Tailoring Pore Structures of 3D Printed Cellular High-Loading Cathodes for Advanced Rechargeable Zinc-Ion Batteries

Hui Ma, Xiaocong Tian, Teng Wang, Kang Tang, Zixian Liu, Shuen Hou, Hongyun Jin,* and Guozhong Cao*

Developing high-loading cathodes with superior electrochemical performance is desirable but challenging in aqueous zinc-ion batteries (ZIBs) for commercialization. Advanced 3D printing of cellular and hierarchical porous cathodes with high mass loading for superior ZIBs is explored here. To obtain a high-performance 3D printable ink, a composite material of iron vanadate and reduced holey graphene oxide is synthesized as the ink component. A cellular cathode with hierarchical porous architecture for aqueous ZIBs is then designed and fabricated by 3D printing for the first time. The unique structures of 3D printed composite cathode provide interpenetrating transmission paths as well as channels for electrons and ions. 3D printed cathodes with high mass loading over 10 mg cm^{-2} exhibit a high specific capacity of 344.8 mAh g^{-1} at 0.1 A g^{-1} and deliver outstanding cycling stability over 650 cycles at 2 A g^{-1}. In addition, the printing strategy enables the ease increase in mass loading up to 24.4 mg cm^{-2}, where a remarkably high areal capacity of 7.04 mAh cm^{-2} is reached. The superior electrochemical performance paves the new way to design the state-of-the-art cathodes for ZIBs.

1. Introduction

Multivalent-ion batteries (Mg^{2+}, Zn^{2+}, Ca^{2+}, Al^{3+}, etc.) have attracted ever-increasing attention due to their low cost, environmentally friendly, and high safety.[1–6] Among these batteries, zinc-ion batteries have the outstanding and practical merits due to the advantages of zinc such as a redox potential (−0.76 V vs standard hydrogen electrode), a high theoretical capacity of 820 mAh g^{-1}, and a high volumetric capacity of 5851 mAh mL^{-1}. Compared with lithium-ion batteries (LIBs), aqueous electrolytes possess great advantages including high ionic conductivity, high security, and economy, making them great choice for wearable and portable devices.[7–9]

At present, most reported cathode materials in ZIBs are manganese-based compounds, vanadium-based compounds, Prussian blue analogs and some organic metal compounds.[10–14] Among these cathodes, vanadium-based compounds are one of the most promising candidates for grid-scale energy storage due to their stability and high capacity.[15] Although various layered vanadate (such as $Zn_3V_2O_7(OH)_2 \cdot 2H_2O$,[16] $NaV_3O_8 \cdot 1.5H_2O$,[17] $Na_2V_6O_{16} \cdot 1.63H_2O$,[18] $CaV_6O_{16} \cdot 3H_2O$,[19] etc.) have been widely investigated as high-capacity cathodes in ZIBs, most cathodes suffer from low mass loading and their electrode configurations are largely restricted due to the used traditional coating method.[20–22] Some fabrication methods such as 3D printing have been explored to obtain desirable electrodes with customized configurations as well as improved electrochemical performance.

3D printing, also termed as additive manufacturing, is widely used to fabricate high-performance materials and devices in various fields such as energy storage, electronic, and biotechnology. It possesses unique manufacturing advantages including customized design, rapid prototyping, and structural optimizing.[23,24] It includes stereolithography, direct ink writing (DIW), fused deposition modeling, selective laser melting, selective laser sintering, etc.[25,26] Among these techniques, DIW belongs to one of the most commonly used 3D printing techniques due to its ease of use, low-cost, wide range of materials. In addition, it can also construct arbitrarily complex structure whose precision ranges from hundreds of micrometers to nanometers. It provides an ideal platform to build electrodes and tune their electrochemical behaviors for many energy storage devices such as LIBs, Li–S batteries, supercapacitors,

H. Ma, Prof. X. Tian, K. Tang, Z. Liu, Prof. S. Hou, Prof. H. Jin
Engineering Research Center of Nano-Geo Materials of Ministry of Education Faculty of Materials Science and Chemistry
China University of Geosciences
Wuhan 430074, P. R. China
E-mail: tianxc@cug.edu.cn; jinhongyun@cug.edu.cn

Prof. X. Tian
Zhejiang Institute
China University of Geosciences
Hangzhou 311305, P. R. China

T. Wang
The Institute of Technological Sciences
Wuhan University
Wuhan 430072, P. R. China

Prof. G. Cao
Department of Materials Science & Engineering
University of Washington
Seattle, WA 98195, USA

The ORCID identification number(s) for the author(s) of this article can be found under https://doi.org/10.1002/smll.202100746.

DOI: 10.1002/smll.202100746

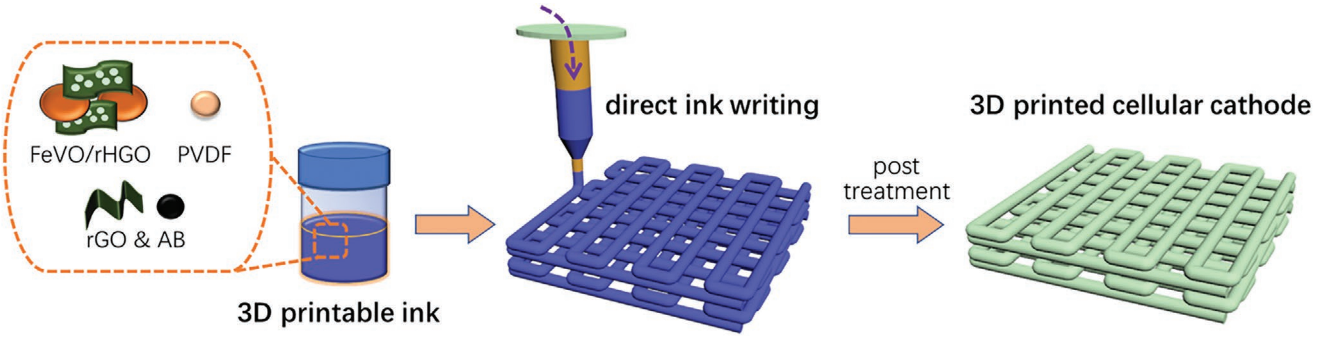

Figure 1. Schematic of DIW-based fabrication of cellular FeVO/rHGO cathodes for ZIBs.

and ZIBs.[23,27–30] For example, Sun et al. reported nanocomposite gel-based thick electrode for high-performance LIBs.[31] Chen et al. designed a wearable Li–S bracelet battery using the 3D printing technology.[32] However, it is imminently needed but remains challenging to elaborate desirable cathodes and achieve both high electrochemical performance and high mass loading for low-cost energy storage systems such as ZIBs.

This study explored a DIW of cellular cathodes with high mass loading for ZIBs. A nanocomposite ink consists of $Fe_5V_{15}O_{39}(OH)_9 \cdot 9H_2O$ (FeVO) nanosheets and reduced holey graphene oxide (rHGO) as active materials for the cellular cathode. 3D printable ink with well controlled rheological properties was extruded onto various substrates, and subsequently formed free-standing nanocomposite cathodes. Such 3D printed cathodes containing periodic open macroporous channels and hierarchical porostructures synergistically facilitated infiltration of electrolyte ions and greatly enhanced rapid transport of electrons and ions. 3D printed FeVO/rHGO (3DP-FeVO/rHGO) cathode delivered an initial discharge capacity of 344.8 mAh g^{-1} at 0.1 A g^{-1}, excellent rate performance, and stable cycling stability (126.4 mAh g^{-1} over 650 cycles at 2 A g^{-1}) even at a high mass loading of ≈12.4 mg cm^{-2}. The results represent an advanced proof of concept for 3D printing toward ZIBs and also a popularized platform for next-generation state-of-the-art energy storage devices.

2. Results and Discussion

The DIW-based printing process is illustrated in **Figure 1**. In the first step, active material (FeVO/rHGO) and conductive additive (reduced graphene oxide (rGO) and acetylene black (AB)) were well-mixed with binder (polyvinylidene fluoride (PVDF)) and solvent (*N*-methyl pyrrolidone (NMP)) to form the uniform, high-viscous, thixotropic composite ink, which was extruded from a syringe smoothly onto substrates. In the second step, the post treatment including soaking and freeze drying was employed and the dried films were released from substrates. The resultant free-standing cathodes were thus obtained without the collapse of the overall cathode architecture. It is worth noting that, using the unique DIW-based printing, the electrode configuration could be easily set as a cellular one, and the internal chemical components could be tuned as well. For the optimized electrochemical behaviors, FeVO/rHGO-based formulation was obtained in this work as the cathode for ZIBs.

Figure 2a,b shows the X-ray diffraction (XRD) patterns and Raman spectra of FeVO, FeVO/rGO, and FeVO/rHGO. All of the characteristic peaks of FeVO, FeVO/rGO, and FeVO/rHGO were well indexed to the monoclinic crystalline phase of kazakhstanite (PDF No. 46–1334) and no other impure characteristic peaks were detected (Figure 2a), indicating that the addition of GO and HGO had no effect on the major phase.[33] Two strong peaks located at 8.4° and 25.55° could be corresponding to (002) and (006) directions, which are in accordance with typical (00l) reflections for the bilayer structure. Raman spectra of FeVO, FeVO/rGO, and FeVO/rHGO are displayed in Figure 2b. The peak at 152.7 cm^{-1} was attributed to the skeleton bent vibration. The peaks located at 271.3, 510.5, 704.5,and 766.9 cm^{-1} could be assigned to stretching and bending vibration of V—O bond.[34–37] Another two peaks displaying in FeVO/rGO and FeVO/rHGO at 1344.5 and 1605.8 cm^{-1} were indexed to D band and G band of rGO and rHGO. I_D/I_G ratio of FeVO/rHGO increased compared with that of HGO as shown in Figure S1 in the Supporting Information, implying the reduction process during the composite synthesis.[38]

The morphologies of FeVO/rHGO and FeVO/rGO were further observed as shown in Figure 2c and Figure S2 in the Supporting Information. Both FeVO/rHGO and FeVO/rGO displayed the typical nanosheet morphologies where the sheet thickness was thin without an obvious agglomeration. Transmission electron microscopy (TEM) images of FeVO/rHGO and FeVO/rGO shown in Figure 2d and Figure S3 in the Supporting Information further confirmed the typical nanosheet structure. FeVO nanosheets and rHGO (or rGO) were entirely covered by each other. As shown in the high-resolution TEM (HRTEM) image (Figure 2e,f), the measured lattice spacings of 0.209 and 0.197 nm corresponded to the d_{0010} and d_{-513} spacing of FeVO, respectively. In addition, the microstructure of FeVO/rHGO, FeVO/rGO, and FeVO was measured by nitrogen adsorption/desorption as displayed in Figure S4 in the Supporting Information. The surface areas of FeVO/rHGO, FeVO/rGO, and FeVO were 64.6, 50.6, and 28.5 m^2 g^{-1}, respectively, implying the contribution of holey nanosheets. The energy-dispersive spectrometer (EDS) elemental mapping of FeVO/rHGO illustrated the homogeneous element distributions of Fe, V, C, and O, as displayed in Figure 2g and Figure S5 in the Supporting Information.

One of the most challenging elements for constructing 3D printed electrodes is to develop printable inks with good rheological behaviors and desirable formulation. As shown in

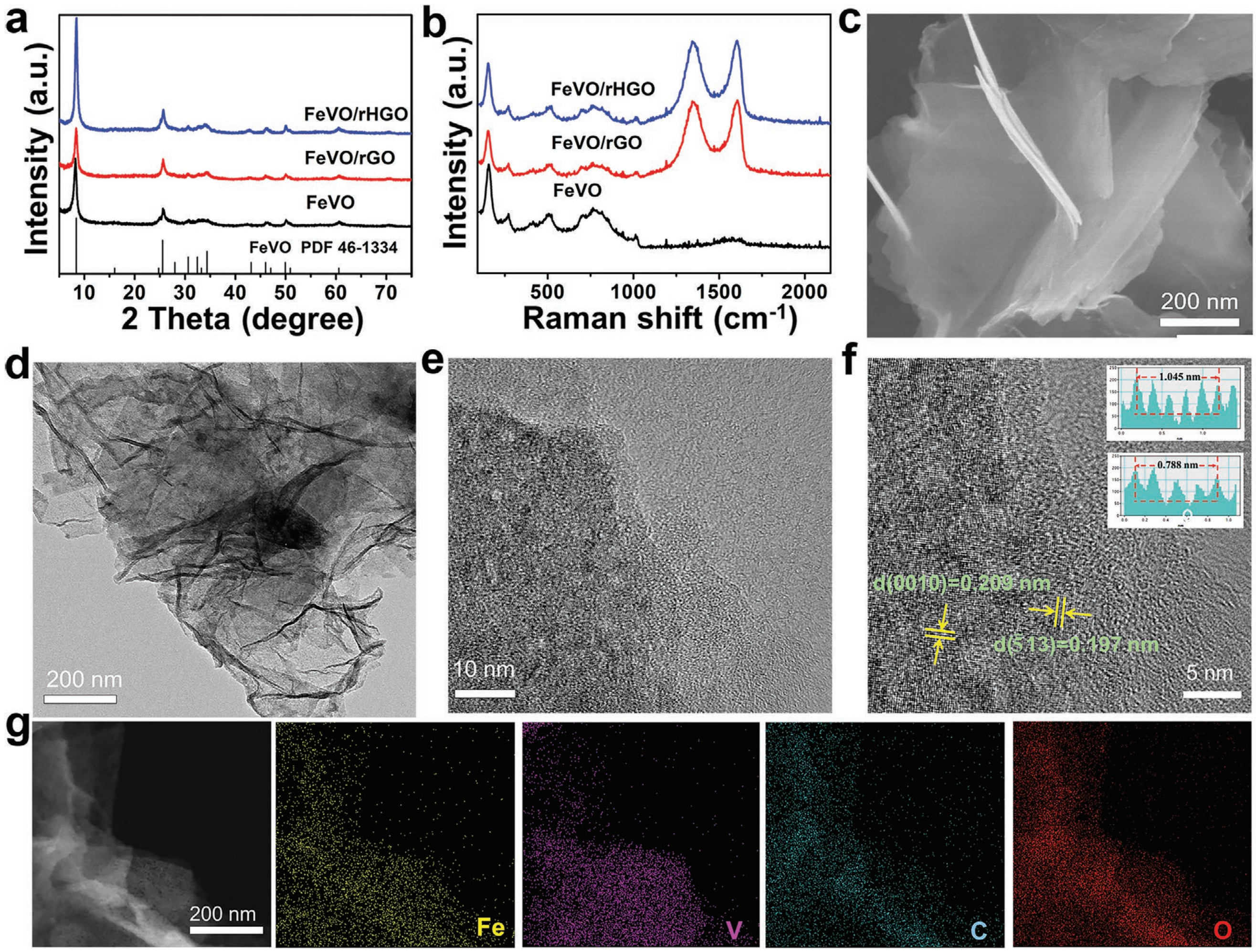

Figure 2. a) XRD pattern and b) Raman spectra of as-prepared FeVO/rHGO, FeVO/rGO and FeVO sample. c) SEM image, d) TEM image, e,f) HRTEM image, and corresponding g) EDS elemental mappings of FeVO/rHGO sample.

Figure 3a, the prepared ink located at the bottle bottom did not flow down along the bottle wall when the bottle was turned down for 48 h, reflecting a self-supporting behavior of the obtained ink. The continuous ink extrusion state also revealed the good fluidity behavior. By regulating printing routes, 3D printed cellular electrodes with different layers can be easily fabricated without changing the cellular configuration. To further understand the fluidity of the ready ink, the rheological behavior of the prepared FeVO/rHGO ink was investigated. As displayed in Figure 3b and Figure S6 in the Supporting Information, the high-viscosity ink exhibited the shear-thinning non-Newtonian fluid behavior and the stable ink flowing property.

The microstructure of 3D printed cathodes was studied by scanning electron microscopic (SEM) images. It can be found that the 3DP-FeVO/rHGO and 3D printed FeVO/rGO (3DP-FeVO/rGO) cathodes were composed of interwoven horizontal and vertical columns with a diameter of ≈390 µm (Figure 3c; Figure S7, Supporting Information). The space caused by intersecting and adjacent columns can offer channels for the permeation of electrolyte ions. From a cross-sectional view (Figure 3d), the upper layer and the lower layer were stacked closely, and cylinder columns were clearly observed. After the post treatment, the porous framework was formed for 3DP-FeVO/rHGO and 3DP-FeVO/rGO cathodes (Figure 3e; Figure S7, Supporting Information). The periodic macroporous structure facilitated the permeation of electrolyte ions and ensured the rapid ion transport, which is highly important for thick electrodes. It reflected one of manufacturing advantages for 3D printing technology in the field of energy storage. Particularly, the employed DIW-based 3D printing has more distinct advantages with easy to operation and economy. As displayed in Figure 3f, FeVO was surrounded by rHGO nanosheets for the 3DP-FeVO/rHGO cathode. As demonstrated in Figure 3g, our electrode materials with different geometric shapes, a labyrinth pattern and various letter patterns could all be printed onto diverse substrates such as hard glass, flexible polyethylene terephthalate (PET), stainless-steel foil, and paper, presenting the versatility of the DIW-based 3D printing technique.

In order to evaluate the electrochemical performance of 3D printed cathodes, coin cells were assembled where free-standing 3D printed cathodes with two printing layers (mass loading over 10 mg cm^{-2}) were firstly used as the cathode, and zinc foil

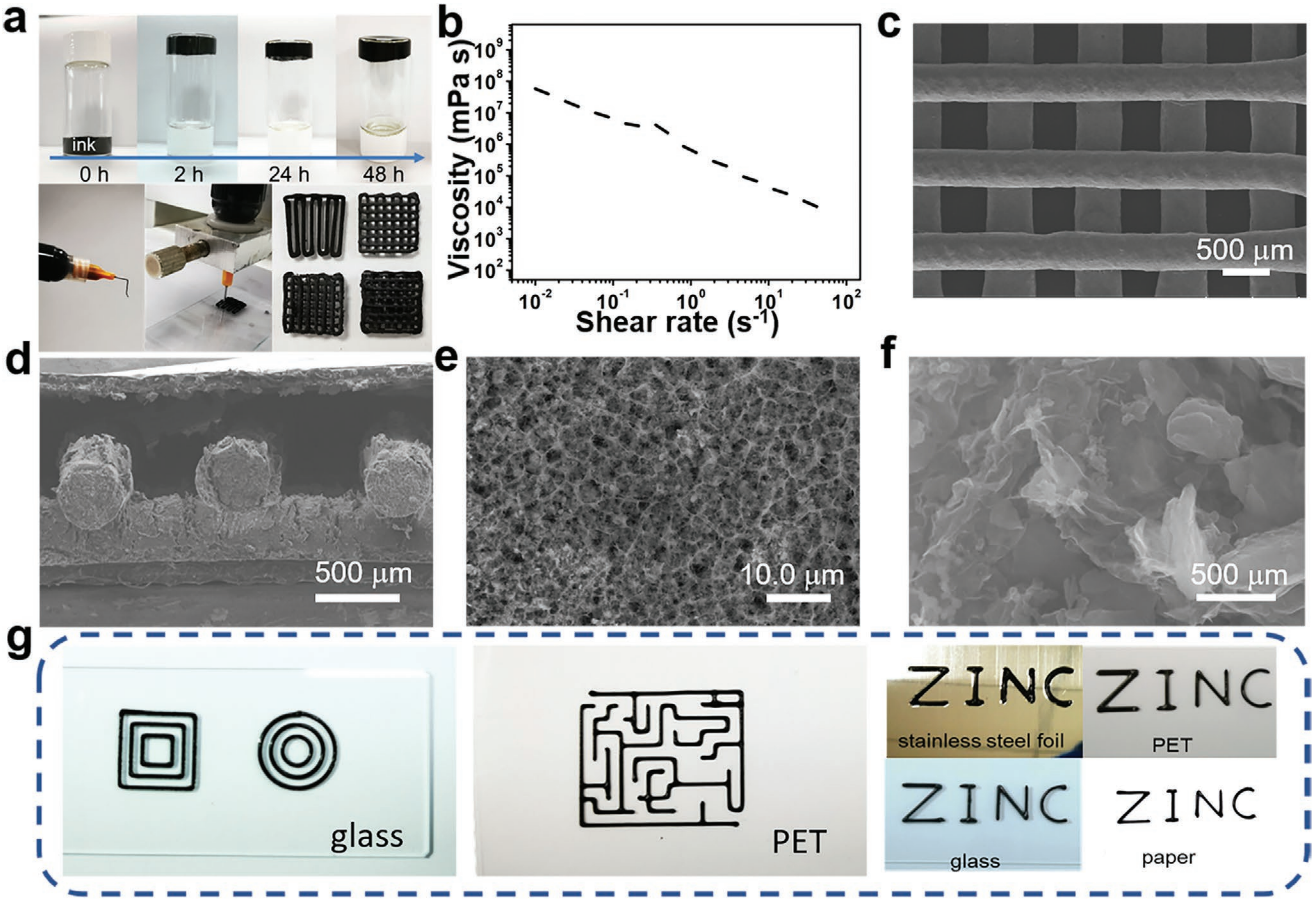

Figure 3. a) Photographs of printable ink, printing syringe, and printed patterns with different layers. b) Rheological properties of FeVO/rHGO inks. c) Top-viewed, d) cross-sectional and e,f) magnified SEM images of 3DP-FeVO/rHGO cathodes. g) Photographs of 3D printed materials with various patterns onto different substrates.

was employed as the anode. **Figure 4**a shows a cyclic voltammetry (CV) curve of 3DP-FeVO/rHGO cathodes in the voltage range of 0.4–1.6 V at a scan rate of 0.1 mV s^{-1}. The reduction peak at ≈0.73 V was attributed to the insertion of Zn^{2+} into cathodes. Two oxidation peaks at ≈0.75 and ≈1.10 V were attributed to the extraction of Zn^{2+} from the cathodes.[33] CV curves of 3DP-FeVO/rGO and 3D printed FeVO (3DP-FeVO) cathodes at a scan rate of 0.1 mV s^{-1} were found to be similar as shown in Figure S8 in the Supporting Information, indicating the similar electrochemical reaction processes. Figure 4b shows the galvanostatic charge–discharge (GCD) curves of various 3D printed cathodes for the first cycle at a current density of 0.1 A g^{-1}. All 3D printed cathodes presented the similar discharge (Zn^{2+} ions insertion) and charge (Zn^{2+} ions extraction) behaviors for the first cycle. However, for the 3DP-FeVO cathode, a higher platform was observed during the charge process than those of 3DP-FeVO/rGO and 3DP-FeVO/rHGO cathodes, indicating the large polarization and high hysteresis of 3DP-FeVO cathode. It may be caused by low electrical conductivity of pristine FeVO. Under high mass-loading, the 3DP-FeVO/rHGO cathodes exhibited high discharge and charge capacities of 344.8 and 336.4 mAh g^{-1}, respectively, at a current density of 0.1 A g^{-1}, which were superior to those of 3DP-FeVO/rGO (336.7 and 318.3 mAh g^{-1}) and 3DP-FeVO cathodes (320.6 and 301.2 mAh g^{-1}), demonstrating the obvious enhancement in the electrochemical reaction activity and capacity with the presence of rGO and rHGO in the high mass-loading electrodes.

The rate performance of obtained three kinds of 3D printed cathodes at a series of current densities ranging from 0.4 to 2.0 A g^{-1} was displayed to further assess the electrochemical behaviors. As shown in Figure 4c, the discharge capacities of 3DP-FeVO/rHGO cathodes were 259.7, 210.0, 188.0, 143.9, and 114.1 mAh g^{-1} at the current densities of 0.4, 0.8, 1.0, 1.5, and 2.0 A g^{-1}, respectively. When the current density came back to 0.4 A g^{-1}, the discharge capacity recovered to a high capacity at 261.3 mAh g^{-1}. At different current densities, corresponding GCD curves of 3DP-FeVO/rHGO cathodes at various current densities showed the similar plateau as displayed in Figure 4d. In comparison, at a high current density of 2 A g^{-1}, the discharge capacities of 3DP-FeVO/rGO and 3DP-FeVO cathodes decreased sharply to 96.4 and 71.5 mAh g^{-1}, respectively. When the current density resumes to 0.4 A g^{-1}, 3DP-FeVO/rGO and 3DP-FeVO cathode showed inferior discharge capacities of 252.6 and 189.9 mAh g^{-1}, respectively. Those results were a clear indication that 3DP-FeVO/rHGO cathodes demonstrated a much better rate capability compared with 3DP-FeVO/rGO and 3DP-FeVO ones. It may be due to the presence of rationally designed pores inner 3DP-FeVO/rHGO cathodes, where

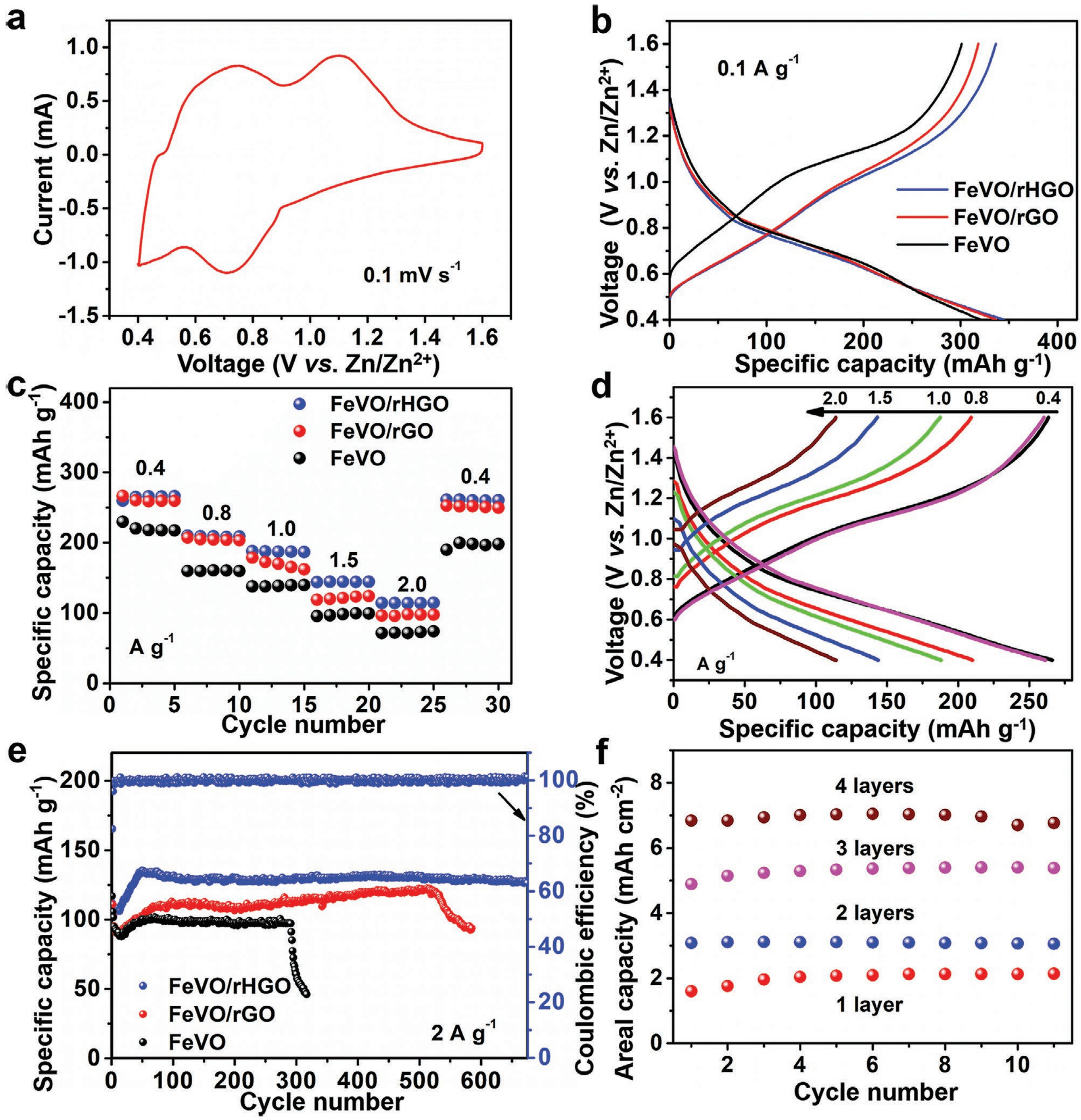

Figure 4. a) CV curve of 3DP-FeVO/rHGO cathodes at a scan rate of 0.1 mV s^{-1}. b) GCD profiles at a current density of 0.1 A g^{-1} and c) rate performance for obtained various 3D printed cathodes. d) GCD profiles of 3DP-FeVO/rHGO cathodes at different current densities. e) Long-term cycling performance at a current density of 2 A g^{-1}. f) Areal capacities of 3DP-FeVO/rHGO with different printing layers at a current density of 6 mA cm^{-2}.

more ion channels were thus provided to facilitate the rapid ion diffusion.

Long-term cycling performance was further tested to evaluate the electrochemical stability of various 3D printed cathodes as demonstrated in Figure 4e. At a current density of 2 A g^{-1}, 3DP-FeVO/rHGO cathodes still delivered a high discharge capacity of 112.1 mAh g^{-1} for the first cycle. During the initial 50 cycles, the discharge capacities were gradually increased to 135.5 mAh g^{-1}, which may be attributed to the electrode activation process. This activation process also happened for 3DP-FeVO/rGO and 3DP-FeVO cathodes. It can be seen that 3DP-FeVO/rHGO cathodes displayed a superior long-term cycle life with a high capacity of 126.4 mAh g^{-1} even after 675 cycles, corresponding to outstanding capacity retention up to 93.3% based on the observed maximum capacity. In comparison, 3DP-FeVO/rGO and 3DP-FeVO cathodes exhibited much lower capacities of 93.8 mAh g^{-1} after 585 cycles and 85.2 mAh g^{-1} after 293 cycles, respectively. Moreover, as the cycling continued, the capacities of 3DP-FeVO/rGO and 3DP-FeVO cathodes decayed at a much faster rate and then obtained cells suddenly went to failure soon.

To further demonstrate the flexible control in the electrode mass loading and confirm the advantageous practical value of the utilized 3D printing, the operation with increased printing layers was also performed for 3DP-FeVO/rHGO cathodes. With the increase in printing layers, the areal capacities of 3DP-FeVO/rHGO cathodes increased accordingly as shown in Figure 4f. With a growing increase of printing layer up to 4, the electrode mass loading level grew up to 24.4 mg cm^{-2}, which was remarkably high compared with those of previously reported vanadium-based cathodes.[39–43] At such a high mass loading level, the areal capacity of 3DP-FeVO/rHGO cathodes reached 7.04 mAh cm^{-2} at a current density of 6 mA cm^{-2}. It worth noting that the volumetric capacity of our 3D printed cellular cathode-based battery were still superior to previously reported ones (Table S1, Supporting Information). It indicated that the ultrahigh areal specific capacity of electrodes and ultrahigh volumetric energy density of Zn-ion battery could be accessed through the unique DIW-based 3D printing. Apart from the excellent electrochemical performance, the mechanical properties of 3DP-FeVO/rHGO were also studied. As shown in Figure S9 in the Supporting Information, 3DP-FeVO/rHGO remained intact after the battery cycling test, illustrating a good mechanical strength when assembling or using.

To further understand the electrochemical kinetics of 3DP-FeVO/rHGO cathodes, CV curves of at multiple scan rates from 0.2 to 0.7 mV s^{-1} were shown in Figure S10a in the Supporting Information. It was worth noting that the area of the CV curves increased as the scan rate increased. Meanwhile, the capacitive effect of 3DP-FeVO/rHGO cathode can be described from the following equation[44]

$$i = av^b \tag{1}$$

where i is the current, v is the scan rate, and a and b are adjustable parameters. According to the linear fitting graph of log(i) versus log(v) as displayed in Figure S10b in the Supporting Information, the values of the peak 1 and peak 2 were 0.72 and 0.54, respectively. This result indicated that Zn^{2+} storage process was synergistically controlled by capacitive and diffusion process. Galvanostatic intermittent titration technique (GITT) test was also carried out to determine Zn^{2+} ions diffusion coefficient in 3DP-FeVO/rHGO cathodes as shown in Figure S11a in the Supporting Information. The Zn^{2+} ions diffusion coefficient (D) can be calculated according to the following equation[33]

$$D = \frac{4}{\pi\tau}\left(\frac{m_B V_M}{M_B S}\right)^2 \left(\frac{\Delta E_S}{\Delta E_t}\right)^2 \tag{2}$$

where τ, m_B, V_M, and M_B represent current pulse time, the mass, molar volume, and molar mass of the active material, respectively. S means the contact area of the electrodes and the electrolyte; ΔE_S and ΔE_t correspond to voltage change of the steady-state under the current pulse and under the constant current pulse after eliminating the IR drop, respectively. The diffusion coefficient was calculated around 10^{-9} cm^2 s^{-1} as shown in Figure S11b in the Supporting Information, which was dynamically changing and higher than those of reported vanadium-based cathodes.[45–47] Electrochemical impedance spectra (EIS) measurements were also applied to verify the diffusion behaviors of charges as seen in Figure S12 in the Supporting Information. The charge-transfer resistance (R_{ct}) of 3DP-FeVO/rHGO cathodes after first cycle was smaller than those of 3DP-FeVO/rGO and 3DP-FeVO cathodes. This may be due to the rationally designed pores in 3DP-FeVO/rHGO electrodes, which allowed for the rapid electrical and ionic transport. In addition, the value of R_{ct} for the 3DP-FeVO/rHGO cathodes dropped after the 50th and 200th cycles, implying the activation process of electrodes for initial charge and discharge cycles.

In order to reveal the electrochemical reaction during the charge and discharge process for 3DP-FeVO/rHGO cathodes, ex situ XPS measurements were conducted at the original, discharged (0.4 V) and charged states (1.6 V) for the first cycle and the fitting results were shown in **Figure 5**a–c. At the discharged state, the V^{5+} peak and V^{4+} peak shifted to higher binding energy values at about 517.8 and 517.5 eV respectively possibly due to the insertion of Zn^{2+} ions and the recombination of V^{4+}/V^{5+}. The V^{5+} peak became weaker and the V^{4+} peak became stronger. A new peak about 516.4 eV corresponded to V^{3+} displayed at higher relative intensity than that of the peak for V^{4+}, indicating that V^{5+} was partially reduced to V^{4+} and V^{3+} during the discharge process. At the charged state, V^{3+} and V^{4+} was oxidized to V^{5+}, indicating the high reversibility of V element during cycles.[16,33,48] The similar phenomenon happened for Fe $2p_{3/2}$ spectra, where Fe^{3+} was reduced at discharge process and Fe $2p_{3/2}$ spectra returned to the original state after charging.[33,49] Zn 2p elemental spectra further confirmed the reversibility of the insertion and extraction of Zn ions during discharge and charge processes. Two strong peaks at ≈1045.3 and 1022.3 eV corresponding to Zn $2p_{1/2}$ and Zn $2p_{3/2}$ at the discharged state provided the powerful evidence of inserted Zn ions in 3DP-FeVO/rHGO. The intensity of the two peaks obviously decreased at the charged state, indicating the extraction of Zn^{2+} as well as the good reversibility. The residual Zn ions may be attributed that a small quantity of Zn ions cannot be extracted during the charge process, which may result in the capacity decay during the long cycles.[50]

Ex situ XRD study was also conducted to further investigate the reaction mechanism of 3DP-FeVO/rHGO cathodes for the first discharge–charge cycle (Figure 5d–f). Along with the discharge process, the diffraction peaks at 8.4° corresponding to (002) plane showed a slightly shift to higher angles, suggesting the shrinkage of interlayer spacing. This may be attributed to the electrostatic attractions and the resulting hydrogen bonds between inserted Zn^{2+} with layered skeleton.[48] Upon the charge process, the (002) peak almost returned to the original position. It suggested that the structural change was greatly reversible which could ensure the good cycling stability. In addition, the peaks at 6.5°, 13.1°, 17.2°, 24.2°, and 24.7° appeared when the discharge process operated from 0.8 to 0.4 V and disappeared as the charge process operated from 0.4 to 0.8 V. It was possibly due to the formation of zinc salts $Zn_x(OH)_y(CF_3SO_3)\cdot nH_2O$ during the discharge–charge process when the electrolyte was $Zn(CF_3SO_3)_2$ solution.[36,41]

For energy storage electrodes, the electrochemical behaviors correlated closely with the mass loading level. To access the

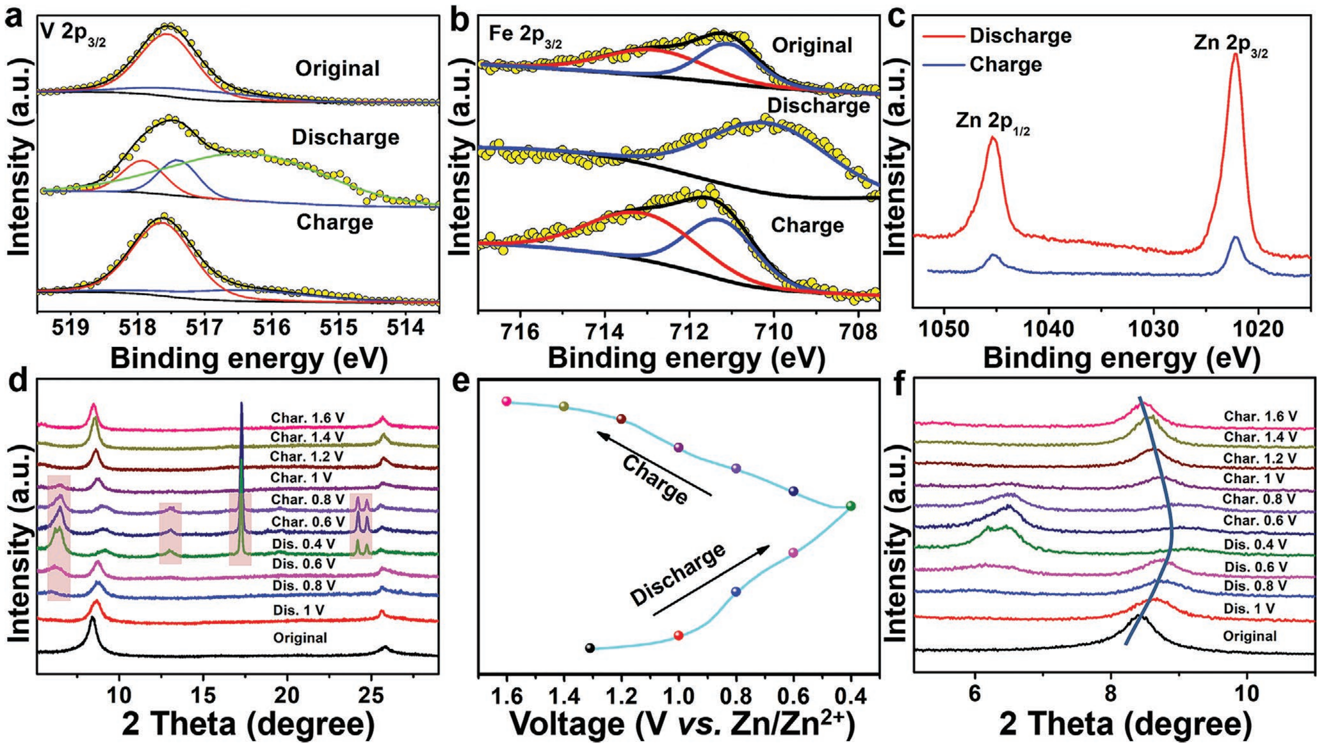

Figure 5. XPS spectra of 3DP-FeVO/rHGO cathodes for a) V $2p_{3/2}$, in which V^{5+} is red, V^{4+} is blue, and V^{3+} is green; b) Fe $2p_{3/2}$, in which Fe^{3+} is red, Fe^{2+} is blue; c) Zn 2p in original, fully discharged, and charged states. d–f) Ex situ XRD characterization of 3DP-FeVO/rHGO cathodes at the first cycle.

practical application and elaborate high-performance thick electrodes, our 3D printing strategy provided an ideal platform to tailoring the electrode configurations for ZIBs. **Figure 6** shows a clear illustration that 3D printed cellular structure could offer open channels as well as large contact with electrolyte, leading to a 3D migration for ions throughout the whole electrode architecture. However, it was worth noting that the inner structure of 3D printed electrodes also significantly mattered for the delivered electrochemical behaviors. With the introduction of rGO and rHGO nanosheets, the interconnected and conductive 3D network could boost the electrical transport and offer more active sites. With the further tailoring in nanosheet

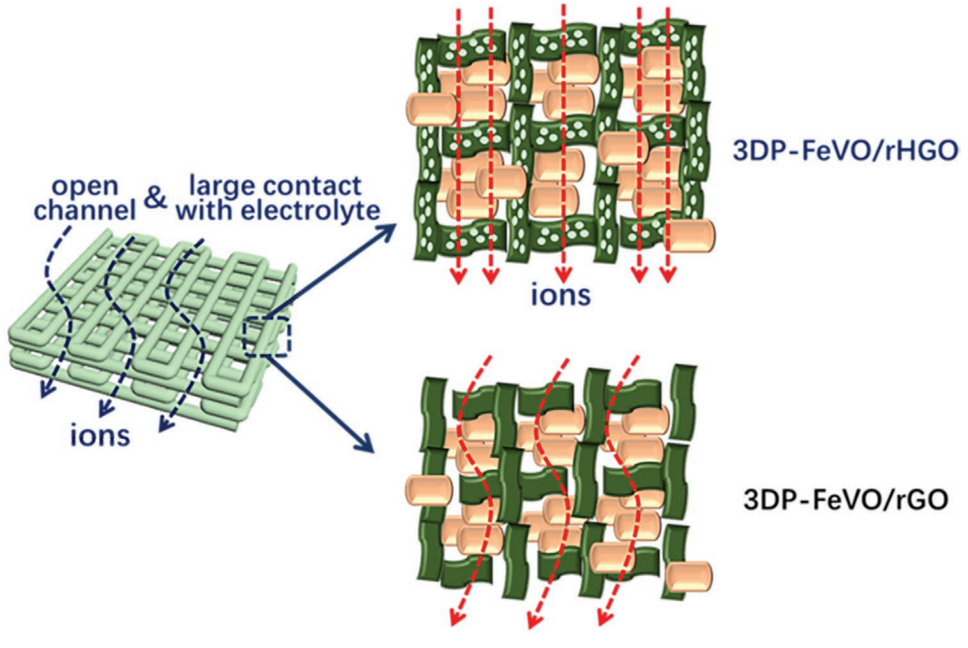

Figure 6. Schematic of ionic transport for 3D printed FeVO/rHGO and FeVO/rGO electrodes.

in-plane pores, rHGO allowed for more sufficient ion diffusion for 3D printed electrodes compared with the rGO-introduced ones. With the combination of 3D printing control in electrode configuration and pores tailoring, our 3D printed FeVO/rHGO electrodes enabled desirable electrical and ionic transport, resulting in the remarkable electrochemical behaviors even at practical high mass loading levels.

3. Conclusion

In summary, cellular high-loading 3DP-FeVO/rHGO cathodes were fabricated by means of a unique DIW-based 3D printing with FeVO/rHGO-based 3D printable ink. The resulting electrodes consist of tailored hierarchical porostructures, and such 3DP-FeVO/rHGO cathodes with high mass loading (>10 mg cm^{-2}) delivered a high specific capacity of 344.8 mAh g^{-1} at 0.1 A g^{-1}, excellent rate performance (114 mAh g^{-1} at 2 A g^{-1}), and long-term cycling stability (126.4 mAh g^{-1} over 650 cycles at 2 A g^{-1}). In addition, the mass loading of 3DP- FeVO/rHGO cathodes with four printing layers reached 24.4 mg cm^{-2}, while a remarkably high areal capacity of 7.04 mAh cm^{-2} was still manifested at a current density of 6 mA cm^{-2}. The superior electrochemical behaviors may be attributed to the desirable electrical and ionic transport in 3D printed electrodes. This work implies great potential of 3D printing in designing and fabricating state-of-the-art high-loading electrodes for next-generation advanced energy storage.

4. Experimental Section

Synthesis of FeVO/rHGO: HGO was first obtained prior to the synthesis of FeVO/rHGO. In a typical procedure,[51] the graphene oxide (GO) suspension (12 mL, 10 mg mL^{-1}, XF NANO) was directly used and mixed with 65–68% concentrated HNO_3 with the volume ratio of 1:10. Then, the mixture was sonicated in a bath sonicator at room temperature for 2 h. After sonication, the mixture was settled for 1 h at room temperature and centrifuged with water for several times to remove the acid. The resultant sample was labeled as HGO.

FeVO/rHGO was subsequently synthesized by a simple water bath method. In a typical procedure,[33] 0.701 g NH_4VO_3 was added in 200 mL deionized water, and stirred at 90 °C. Then HGO was added into the solution with vigorous stirring for 30 min. 20 mL of 0.1 м Fe $(NO_3)_3$ solution was dropwise added into the above solution and kept at 90 °C for 4 h to form the brown precipitates. The precipitates were washed by centrifugation with deionized water and pure ethanol and finally dried at 80 °C to obtain FeVO/rHGO. For comparison, FeVO was prepared by the same method without adding of the HGO suspension. FeVO/rGO was also prepared using the same method where GO suspension was employed instead of HGO one.

3D Printing of FeVO/rHGO Electrode: 3D printable ink was formulated by mixing the FeVO/rHGO active material, rGO, AB conductive additive, and PVDF binder with a weight ratio of 7:1:1:1. NMP with suitable amount was used to adjust the viscoelasticity of above mixture for DIW-based printing. The obtained inks were transferred into a syringe with a ≈330 µm diameter needle. A three-axis extrusion system was utilized for the DIW-based printing process following a preprogrammed route under a constant extruding pressure. The initial needle height from the substrate was tuned at around 0.25 mm to ensure the adhesion between the extruded materials and the substrate, and the moving speed of the syringe needle was set at 6 mm s^{-1}. As-printed 3DP-FeVO/rHGO cellular cathodes were dipped into deionized water for 4 h and further freeze-dried for 8 h. 3DP-FeVO/rGO and 3DP-FeVO cellular cathodes were also prepared using the same printing method with same printing parameters.

Structural Characterization and Electrochemical Measurements: XRD measurements were performed to identify the structure of samples by Bruker D8 Discover X-ray diffractometer, using a non-monochromatic Cu Kα radiation (λ = 1.5405 Å). SEM images were observed using a Hitachi SU8010 field-emission scanning electron microscope. TEM, EDS element mapping, and HRTEM images were recorded using a JEM2001F transmission electron microscope. Raman spectra were collected on a Thermo Scientific DXR Raman microscopy system. The rheological curve was collected by Anton Paar MCR101 rheometer. Brunauer–Emmett–Teller (BET) surface areas were measured using the nitrogen adsorption method on Vsorb 2800P.

Zn//FeVO/rHGO, Zn//FeVO/rGO and Zn//FeVO batteries were assembled to CR2025 coin cells in air, where 3DP-FeVO/rHGO, 3DP-FeVO/rGO, and 3DP-FeVO electrodes were used as the cathode, respectively. Glass fiber, metallic Zn foil and 2.5 м $Zn(CF_3SO_3)_2$ were employed as separator, anode, and electrolyte, respectively. CV measurement was conducted on a CHI760E electrochemical workstation at room temperature. GCD and GITT tests were performed on a LANHE CT2001A battery test system with the potential range of 0.4–1.6 V versus Zn/Zn^{2+}. EIS were recorded between 100 kHz and 0.01 Hz on a CHI760E electrochemical workstation.

Supporting Information

Supporting Information is available from the Wiley Online Library or from the author.

Acknowledgements

H.M. and X.T. contributed equally to this work. This work was supported by the National Natural Science Foundation of China (51802292, 21975230), Zhejiang Provincial Natural Science Foundation of China (LY20B010001), Major scientific and technological innovation in Hubei (2019AAA004 and 2018AAA015), Joint Fund of Ministry of Education (6141A02033239), and DONGFENG Project (91224Y180014).

Conflict of Interest

The authors declare no conflict of interest.

Data Availability Statement

Research data are not shared.

Keywords

3D printing, direct ink writing, high mass loading, hierarchical structures, zinc-ion batteries

Received: February 4, 2021
Revised: March 25, 2021
Published online: June 17, 2021

---

[1] H. D. Yoo, Y. Liang, H. Dong, J. Lin, H. Wang, Y. Liu, L. Ma, T. Wu, Y. Li, Q. Ru, Y. Jing, Q. An, W. Zhou, J. Guo, J. Lu, S. T. Pantelides, X. Qian, Y. Yao, *Nat. Commun.* **2017**, *8*, 339.

[2] B. Tang, L. Shan, S. Liang, J. Zhou, *Energy Environ. Sci.* **2019**, *12*, 3288.
[3] C. Xu, B. Li, H. Du, F. Kang, *Angew. Chem., Int. Ed.* **2012**, *51*, 933.
[4] R. J. Gummow, G. Vamvounis, M. B. Kannan, Y. He, *Adv. Mater.* **2018**, *30*, 1801702.
[5] Y. Zhang, S. Liu, Y. Ji, J. Ma, H. Yu, *Adv. Mater.* **2018**, *30*, 1706310.
[6] S. He, J. Wang, X. Zhang, J. Chen, Z. Wang, T. Yang, Z. Liu, Y. Liang, B. Wang, S. Liu, L. Zhang, J. Huang, J. Huang, L. A. O'Dell, H. Yu, *Adv. Funct. Mater.* **2019**, *29*, 1905228.
[7] X. Jia, C. Liu, Z. G. Neale, J. Yang, G. Cao, *Chem. Rev.* **2020**, *120*, 7795.
[8] D. Selvakumaran, A. Pan, S. Liang, G. Cao, *J. Mater. Chem. A* **2019**, *7*, 18209.
[9] M. Song, H. Tan, D. Chao, H. J. Fan, *Adv. Funct. Mater.* **2018**, *28*, 1802564.
[10] F. Wan, Z. Niu, *Angew. Chem., Int. Ed.* **2019**, *58*, 16358.
[11] Y. Zhang, H. Ang, K. N. Dinh, K. Rui, H. Lin, J. Zhu, Q. Yan, *Mater. Chem. Front.* **2021**, *5*, 744.
[12] T. Xiong, Y. Zhang, W. S. V. Lee, J. Xue, *Adv. Energy Mater.* **2020**, *10*, 2001769.
[13] H. Yi, R. Qin, S. Ding, Y. Wang, S. Li, Q. Zhao, F. Pan, *Adv. Funct. Mater.* **2021**, *31*, 2006970.
[14] L. Chen, Q. An, L. Mai, *Adv. Mater. Interfaces* **2019**, *6*, 1900387.
[15] X. Xu, F. Xiong, J. Meng, X. Wang, C. Niu, Q. An, L. Mai, *Adv. Funct. Mater.* **2020**, *30*, 1904398.
[16] C. Xia, J. Guo, Y. Lei, H. Liang, C. Zhao, H. N. Alshareef, *Adv. Mater.* **2018**, *30*, 1705580.
[17] F. Wan, L. Zhang, X. Dai, X. Wang, Z. Niu, J. Chen, *Nat. Commun.* **2018**, *9*, 1656.
[18] P. Hu, T. Zhu, X. Wang, X. Wei, M. Yan, J. Li, W. Luo, W. Yang, W. Zhang, L. Zhou, Z. Zhou, L. Mai, *Nano Lett.* **2018**, *18*, 1758.
[19] Y. Zhang, F. Wan, S. Huang, S. Wang, Z. Niu, J. Chen, *Nat. Commun.* **2020**, *11*, 2199.
[20] B. Sambandam, V. Soundharrajan, S. Kim, M. H. Alfaruqi, J. Jo, S. Kim, V. Mathew, Y.-k. Sun, J. Kim, *J. Mater. Chem. A* **2018**, *6*, 15530.
[21] P. He, G. Zhang, X. Liao, M. Yan, X. Xu, Q. An, J. Liu, L. Mai, *Adv. Energy Mater.* **2018**, *8*, 1702463.
[22] G. Yang, T. Wei, C. Wang, *ACS Appl. Mater. Interfaces* **2018**, *10*, 35079.
[23] X. Tian, J. Jin, S. Yuan, C. K. Chua, S. B. Tor, K. Zhou, *Adv. Energy Mater.* **2017**, *7*, 1700127.
[24] P. Chang, H. Mei, S. Zhou, K. G. Dassios, L. Cheng, *J. Mater. Chem. A* **2019**, *7*, 4230.
[25] X. Tian, K. Zhou, *Nanoscale* **2020**, *12*, 7416.
[26] C.-Y. Lee, A. C. Taylor, A. Nattestad, S. Beirne, G. G. Wallace, *Joule* **2019**, *3*, 1835.
[27] X. Tian, K. Tang, H. Jin, T. Wang, X. Liu, W. Yang, Z. Zou, S. Hou, K. Zhou, *Carbon* **2019**, *155*, 562.
[28] T. Wang, X. Tian, L. Li, L. Lu, S. Hou, G. Cao, H. Jin, *J. Mater. Chem. A* **2020**, *8*, 1749.
[29] D. Kong, Y. Wang, S. Huang, B. Zhang, Y. V. Lim, G. J. Sim, Y. A. P. Valdivia, Q. Ge, H. Y. Yang, *ACS Nano* **2020**, *14*, 9675.
[30] X. Gao, X. Yang, Q. Sun, J. Luo, J. Liang, W. Li, J. Wang, S. Wang, M. Li, R. Li, T.-K. Sham, X. Sun, *Energy Storage Mater.* **2020**, *24*, 682.
[31] C. Sun, S. Liu, X. Shi, C. Lai, J. Liang, Y. Chen, *Chem. Eng. J.* **2020**, *381*, 122641.
[32] C. Chen, J. Jiang, W. He, W. Lei, Q. Hao, X. Zhang, *Adv. Funct. Mater.* **2020**, *30*, 1909469.
[33] Z. Peng, Q. Wei, S. Tan, P. He, W. Luo, Q. An, L. Mai, *Chem. Commun.* **2018**, *54*, 4041.
[34] S. Boukhalfa, K. Evanoff, G. Yushin, *Energy Environ. Sci.* **2012**, *5*, 6872.
[35] C. Liu, Z. Neale, J. Zheng, X. Jia, J. Huang, M. Yan, M. Tian, M. Wang, J. Yang, G. Cao, *Energy Environ. Sci.* **2019**, *12*, 2273.
[36] K. Zhu, T. Wu, K. Huang, *ACS Nano* **2019**, *13*, 14447.
[37] X. Zhou, G. Wu, G. Gao, C. Cui, H. Yang, J. Shen, B. Zhou, Z. Zhang, *Electrochim. Acta* **2012**, *74*, 32.
[38] S. Stankovich, D. A. Dikin, R. D. Piner, K. A. Kohlhaas, A. Kleinhammes, Y. Jia, Y. Wu, S. T. Nguyen, R. S. Ruoff, *Carbon* **2007**, *45*, 1558.
[39] X. Pu, T. Song, L. Tang, Y. Tao, T. Cao, Q. Xu, H. Liu, Y. Wang, Y. Xia, *J. Power Sources* **2019**, *437*, 226917.
[40] J. Shin, D. S. Choi, H. J. Lee, Y. Jung, J. W. Choi, *Adv. Energy Mater.* **2019**, *9*, 1900083.
[41] Y. Liu, Q. Li, K. Ma, G. Yang, C. Wang, *ACS Nano* **2019**, *13*, 12081.
[42] M. Liao, J. Wang, L. Ye, H. Sun, Y. Wen, C. Wang, X. Sun, B. Wang, H. Peng, *Angew. Chem., Int. Ed.* **2020**, *132*, 2293.
[43] F. Liu, Z. Chen, G. Fang, Z. Wang, Y. Cai, B. Tang, J. Zhou, S. Liang, *Nano-Micro Lett.* **2019**, *11*, 25.
[44] J. Wang, J. Polleux, J. Lim, B. Dunn, *J. Phys. Chem. C* **2007**, *111*, 14925.
[45] Y. Zhang, H. Jiang, L. Xu, Z. Gao, C. Meng, *ACS Appl. Energy Mater.* **2019**, *2*, 7861.
[46] W. Zhou, J. Chen, M. Chen, X. Xu, Q. Tian, J. Xu, C.-P. Wong, *RSC Adv.* **2019**, *9*, 30556.
[47] H. Geng, M. Cheng, B. Wang, Y. Yang, Y. Zhang, C. C. Li, *Adv. Funct. Mater.* **2020**, *30*, 1907684.
[48] F. Ming, H. Liang, Y. Lei, S. Kandambeth, M. Eddaoudi, H. N. Alshareef, *ACS Energy Lett.* **2018**, *3*, 2602.
[49] F. Ye, H. Dai, K. Peng, T. Li, J. Chen, Z. Chen, N. Li, *J. Adv. Ceram.* **2020**, *9*, 444.
[50] Y. Li, Z. Huang, P. K. Kalambate, Y. Zhong, Z. Huang, M. Xie, Y. Shen, Y. Huang, *Nano Energy* **2019**, *60*, 752.
[51] X. Zhao, C. M. Hayner, M. C. Kung, H. H. Kung, *ACS Nano* **2011**, *5*, 8739.